JACS
JOURNAL OF THE AMERICAN CHEMICAL SOCIETY
Article
pubs.acs.org/JACS

Fe_5C_2 Nanoparticles: A Facile Bromide-Induced Synthesis and as an Active Phase for Fischer–Tropsch Synthesis

Ce Yang,[†] Huabo Zhao,[‡] Yanglong Hou,*[,†] and Ding Ma*[,‡]

[†]Department of Materials Science and Engineering, College of Engineering, and [‡]College of Chemistry and Molecular Engineering, Peking University, Beijing 100871, China

Supporting Information

ABSTRACT: Iron carbide nanoparticles have long been considered to have great potential in new energy conversion, nanomagnets, and nanomedicines. However, the conventional relatively harsh synthetic conditions of iron carbide hindered its wide applications. In this article, we present a facile wet-chemical route for the synthesis of Hägg iron carbide (Fe_5C_2) nanoparticles, in which bromide was found to be the key inducing agent for the conversion of $Fe(CO)_5$ to Fe_5C_2 in the synthetic process. Furthermore, the as-synthesized Fe_5C_2 nanoparticles were applied in the Fischer–Tropsch synthesis (FTS) and exhibited intrinsic catalytic activity in FTS, demonstrating that Fe_5C_2 is an active phase for FTS. Compared with a conventional reduced-hematite catalyst, the Fe_5C_2 nanoparticles showed enhanced catalytic performance in terms of CO conversion and product selectivity.

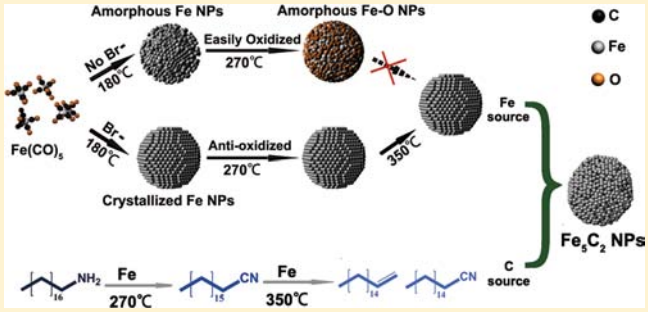

1. INTRODUCTION

For centuries, iron carbides have gained intense interest both in fundamental science and in applied engineering. Primarily, iron carbides consist of carbon atoms occupying the interstices between close-packed iron atoms,[1] and they can be further classified according to whether the carbon atoms are located in trigonal-prismatic interstices (Fe_3C, Fe_5C_2, and Fe_7C_3) or octahedral interstices ($Fe_{2.2}C$ and Fe_2C).[2] In particular, Hägg iron carbide (Fe_5C_2) has a monoclinic unit cell with space group $C2/c$ (a = 11.5620 Å, b = 4.5727 Å, c = 5.0595 Å, and β = 97.74°).[3,4]

The presence of carbon atoms provides iron carbides with excellent mechanical strength and chemical inertness. Therefore, iron carbides have been employed as a crucial component in metallic alloys and hard coating. Indeed, the discovery of iron carbides in ancient Wootz steels in India indicated that iron carbides had been widely used as reinforcement materials 2300 years ago.[5] In contemporary studies, iron carbide nanostructures have been found to possess several unique properties compared with iron or iron oxide nanostructures. For example, the high saturation magnetization (~140 emu/g) and stability make iron carbide nanoparticles (NPs) promising materials in bioimaging[6] and magnetic storage.[7] In addition, iron carbide NPs exhibit excellent catalytic activity in important energy resource conversion processes.[8−19]

Despite their numerous advantages, iron carbide nanostructures have been much less investigated than iron oxide or iron nanostructures, primarily because there are still big challenges in the synthetic strategy of iron carbide nanostructures. Several decades ago, Emmett and co-workers prepared pure-phase iron carbide of micro size via a gas–solid reaction between iron and hydrocarbons.[16,17,19] Stencel and co-workers synthesized iron carbide NPs by a laser pyrolysis method.[20−22] In other reports, nevertheless, iron carbide NPs were mainly observed as a side product during the synthesis of carbon materials.[9,23,24] Antonietti and co-workers recently synthesized Fe_3C nanostructures by a sol–gel method.[6,7,25,26] However, the accompanying high temperature or complicated procedures in current synthetic routes produce iron carbide NPs without control over the size and morphology, which is highly necessary for practical applications.[6,7,23,25−32] In addition, to the best of our knowledge, the synthesis of other iron carbide nanostructures such as Hägg carbide has been rarely reported.

In general, the Fischer–Tropsch synthesis (FTS) can be expressed as nCO + $(2n + 1)H_2 \rightarrow C_nH_{2n+2} + nH_2O$. Since the first report in 1923,[33] FTS has been considered to be a practical approach for producing liquid fuels from fossil resources such as natural gas and coal as well as biomass-derived biogas. Fe- and Co-based catalysts are two major materials in catalytic industry. In particular, Fe-based catalysts have been widely investigated recently because of their low cost, high activity, and capability, and they operate over a wide temperature range (220–350 °C) to produce diesel and wax in low-temperature FTS or gasoline components in high-temperature FTS.[11,34] Though the catalytic mechanism of ferrous materials in FTS is not fully understood, a majority of the available reports have suggested that iron carbides are possibly the active phases of

Received: May 24, 2012
Published: August 31, 2012

   dx.doi.org/10.1021/ja305048p | J. Am. Chem. Soc. 2012, 134, 15814–15821

iron-based catalysts.[10−13,16−19] However, because of the relatively harsh conditions used in preparing iron carbide NPs, typical FTS processes use iron oxide NPs as the catalyst precursors. The catalysts are treated in CO/syngas, at the end of which the oxide NPs are proposed, with controversy, to be transformed into the catalytically active phase, iron carbides, normally as the mixture of various iron carbide phases.[11,14,35] In addition, it was reported that the activity of iron-based catalyst remained almost constant for particle sizes larger than 6 nm, and thus, the intrinsic activity of the iron catalyst is considered to be related more to the phase than to the surface area.[14,36] Therefore, it would be desirable to synthesize single-phase Fe_5C_2 in order to verify its catalytic activity in FTS.

Herein we report a facile chemie douce route for the synthesis of Fe_5C_2 NPs that involves the reaction of iron carbonyl, $Fe(CO)_5$, with octadecylamine in the presence of bromide under mild temperatures (up to 623 K). The size of the iron carbide NPs can be tuned by tailoring the concentration of $Fe(CO)_5$. Most interestingly, the as-synthesized Fe_5C_2 NPs were used as an FTS catalyst, and the results demonstrated that Fe_5C_2 possesses higher activity and selectivity than a conventional reduced-hematite catalyst. More importantly, the induction period observed with conventional iron oxide catalysts was not observed with this catalyst, which clearly indicates that Fe_5C_2 is an active phase for FTS.

2. EXPERIMENTAL SECTION

A classic hot injection strategy was employed to synthesize the Fe_5C_2 NPs. In a typical procedure, octadecylamine was used as both the solvent and surfactant, while cetyltrimethylammonium bromide (CTAB) was used as the inducing agent and $Fe(CO)_5$ as the precursor. Notably, various kinds of bromides were applicable as the inducing agent (Figure S1 in the Supporting Information).

2.1. Synthesis of 20 nm Fe_5C_2 NPs. In a four-neck flask, a mixture of octadecylamine (14.5 g) and CTAB (0.113 g) was stirred sufficiently and degassed under a flow of N_2. The mixture was heated to 393 K, and then $Fe(CO)_5$ (0.5 mL, 3.6 mmol) was injected under a N_2 blanket. The mixture was heated to 453 K at 10 K/min and kept at this temperature for 10 min. A color change from orange to black was observed during the process, implying the decomposition of $Fe(CO)_5$ and the nucleation of Fe nanocrystals. Subsequently, the mixture was further heated to 623 at 10 K/min and kept there for 10 min before it was cooled to room temperature. The product was washed with ethanol and hexane and collected for further characterization. The synthetic procedure for 10 nm NPs was similar to that for 20 nm Fe_5C_2 NPs except that the $Fe(CO)_5$ was dissolved in 2.5 mL of hexane before injection. The as-synthesized NPs were kept in an Ar-filled glovebox to avoid exposure to air before further characterization.

2.2. Characterization. Transmission electron microscopy (TEM) was carried out on an FEI Tecnai T20 microscope. High-resolution TEM (HRTEM) was carried out on an FEI Tecnai F20 microscope. X-ray diffraction (XRD) patterns were obtained using a Rigaku DMAX-2400 X-ray diffractometer equipped with Cu Kα radiation. The accelerating voltage and current were 40 kV and 100 mA, respectively. Extended X-ray absorption fine structure (EXAFS) was characterized on beamline BL14W1-XAFS at the Shanghai Synchrotron Radiation Facility (SSRF), with the storage ring being operated at 3.5 GeV and 300 mA. X-ray photoelectron spectroscopy (XPS) measurements were carried out on an Axis Ultra imaging photoelectron spectrometer (Kratos Analytical Ltd.) using a monochromatized Al Kα anode, and the C 1s peak at 284.8 eV was taken as an internal standard. Raman spectroscopy was recorded on a Renishaw 1000 Raman imaging microscope system with an excitation wavelength of 632.8 nm. Fourier transform IR spectroscopy (FTIR) was carried out on a Nicolet Magna-IR 750 FTIR spectrometer. A gas chromatography−mass spectrometry (GC−MS) instrument (Agilent 7890A GC with a 5975C mass-selective detector) was used to study the synthetic mechanism.

2.3. Catalyst Preparation. To test the catalytic performance of Fe_5C_2 NPs, 80 mg of as-prepared Fe_5C_2 NPs dispersed in ethanol was impregnated with SiO_2 support and dried at room temperature. A supported Fe_2O_3 catalyst was prepared by the impregnation method: an ethanol solution of iron nitrate was added to the SiO_2 support, which was then dried and calcined at 433 K in air. For both catalysts, the loading of Fe was ∼9 wt %.

2.4. FTS Reaction Conditions. The FTS reaction was carried out on a fixed-bed flow reactor with a gas mixture containing 32% CO, 63% H_2, and 5% Ar at a temperature of 543 K. An 80 mg sample of the supported catalyst with ∼9 wt % iron was loaded in a stainless steel tube lined with a quartz layer. The gas hourly space velocity (GHSV) of the reaction was set at 15 000 $cm^3\ h^{-1}\ g_{cat}^{-1}$. For the supported Fe_5C_2 catalyst, no H_2 or CO activation process was adapted. The pressure of the reactor was set at 3 MPa, and the temperature was ramped from 303 to 543 at 3 K/min (the products can be detected immediately as long as the aim temperature was reached). The supported Fe_2O_3 catalyst was first reduced in H_2 at 653 K under 0.1 MPa for 16 h prior to the FTS reaction. When the temperature was reduced to 543 K, the gas flow was switched to syngas, and the pressure was raised to 3 MPa to begin the reaction.

The temperature-programmed surface reaction (TPSR) experiments were performed on the same fixed-bed reactor under the same conditions as for the FTS reaction. The temperature was raised from 303 to 543 K at 3 K/min and then kept at 543 K. The gas flow of the reactor was analyzed using a mass spectrometer (Hiden HPR20). We detected the mass numbers 2 for H_2, 15 for methane, 18 for water, 28 for CO, 41 for propene (to represent the hydrocarbon products), and 44 for CO_2.

2.5. Product Analysis. The product and reactant in the gas phase were detected online using an Agilent 6890 GC. C_1−C_4-ranged alkanes were analyzed using a Plot Al_2O_3 capillary column with a flame ionization detector (FID); CO, CO_2, CH_4, and Ar were analyzed using a Porapak Q- and 5A molecular sieve-packed column with a thermal conductivity detector. The 5% Ar in the syngas was used as an internal standard for the calculation of CO conversion. The product with large molecular weight was collected in a cold trap. Hydrocarbons were analyzed using a 6820 GC with an HP-5 capillary column and an FID, and oxygenates in water were analyzed using a 6820 GC with an HP-INNOWax capillary column and an FID. The selectivity of the products was all on a carbon basis.

3. RESULTS AND DISCUSSION

3.1. Fe_5C_2 Morphology and Structure. The size and morphology of the samples were characterized by TEM. Figure 1a shows that the Fe_5C_2 NPs were ∼20 nm in diameter (Figure S2a). The HRTEM image of an isolated 20 nm Fe_5C_2 NP (Figure 1b) reveals the core−shell structure. The lattice spacing in the core was 0.205 nm, corresponding to the (510) plane of Fe_5C_2, while the shell structure appeared to be amorphous. Moreover, the particle size could be tuned by changing the concentration of $Fe(CO)_5$ in the mixture (Figure S2b,c). The structure of Fe_5C_2 NPs was verified by XRD analysis. Figure 1c shows the XRD pattern of iron carbide NPs (average diameter of 20 nm), which is consistent with that of Fe_5C_2 (JCPDS no. 36-1248). The average particle size estimated from the Scherrer equation was 23.1 nm, which is consistent with the statistical analysis in Figure S2a. EXAFS was used to investigate the fine structure of the samples. For verification, the theoretical Fourier transformed EXAFS (FT-EXAFS) pattern of the first two coordination shells of Fe_5C_2 was fitted using the program IFEFFIT. In Figure 2a, the gray fitted line is a joint contribution of Fe−C scattering in the first Fe−C coordination shell (red circles) and Fe−Fe scattering in the first Fe−Fe coordination shell (blue triangles). The experimental curve is shown in

dx.doi.org/10.1021/ja305048p | J. Am. Chem. Soc. 2012, 134, 15814−15821

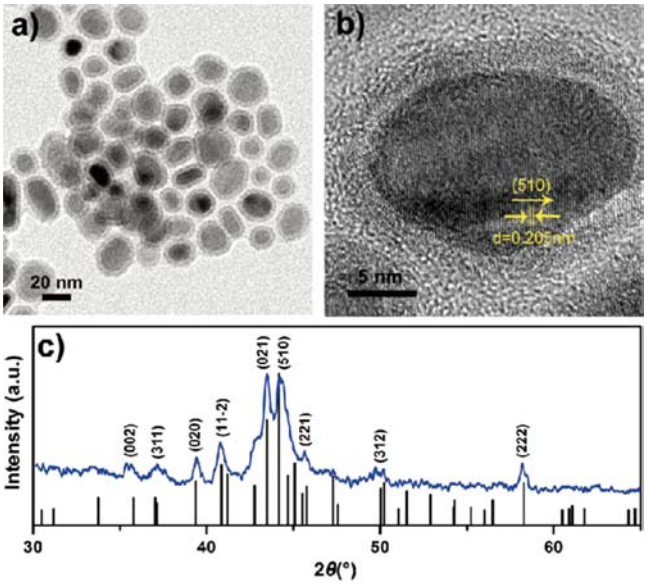

Figure 1. (a) TEM image of 20 nm Fe_5C_2 NPs. (b) HRTEM image of a single 20 nm Fe_5C_2 NP, which reveals that the NP has a core−shell-like structure with a well-crystallized Fe_5C_2 core and an amorphous shell. (c) XRD pattern of 20 nm Fe_5C_2 NPs (JCPDS no. 36-1248).

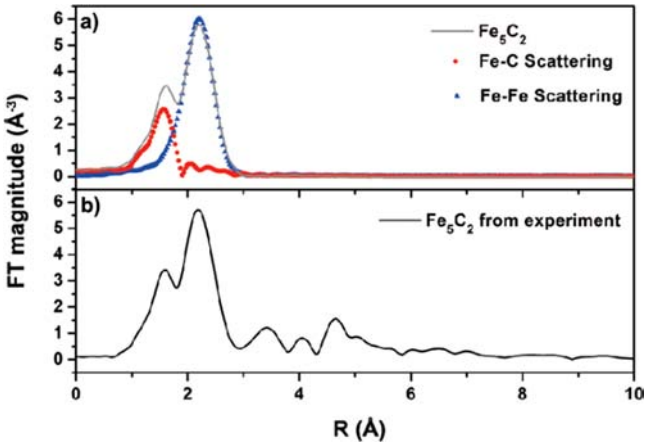

Figure 2. (a) Simulated FT-EXAFS data for Fe_5C_2 (gray solid line) as a sum of contributions from carbon scattering (red ●) and iron scattering (blue ▲). (b) Experimental FT-EXAFS pattern obtained for the Fe_5C_2 NPs.

Figure 2b. The two major peaks at 1.58 and 2.18 Å are in good agreement with the simulated curve. The other peaks in the experimental pattern represent the outer coordination shells of Fe_5C_2. After the correction for phase shifting, the corresponding Fe−C and Fe−Fe bond lengths were determined to be 1.99 and 2.58 Å, respectively.

As mentioned above, the as-synthesized Fe_5C_2 NPs have an amorphous shell. Therefore, XPS and Raman spectroscopy were employed to identify the surface nature of the Fe_5C_2 NPs. The survey XPS spectrum (Figure 3a) shows a C content of 70.55%, an O content of 18.27%, and an Fe content of 9.66%. Furthermore, the two peaks at ∼710 and ∼724 eV in the Fe 2p spectrum (Figure 3b) can be assigned to Fe_3O_4, suggesting the coexistence of a magnetite phase and the carbide phase at the surface.[37] The peak at ∼285 eV in the C 1s spectrum (Figure 3c), combined with HRTEM image, implies the existence of amorphous carbon on the NP surface. In the Raman spectrum

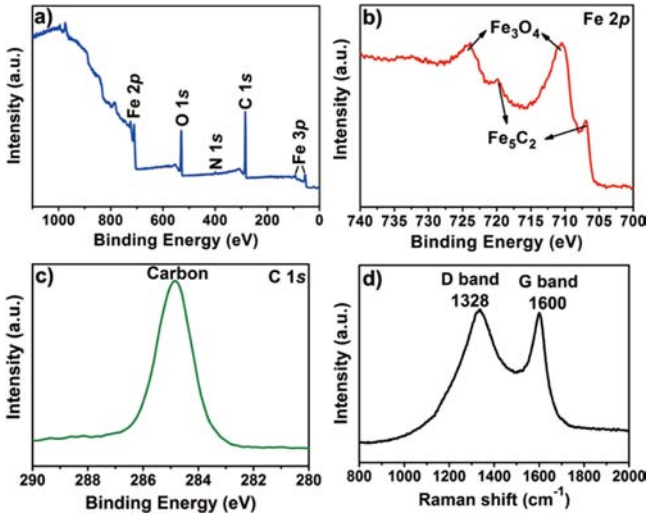

Figure 3. XPS and Raman spectra of the Fe_5C_2 NPs. (a) XPS survey spectrum of Fe_5C_2 NPs showing the presence of carbon and oxygen on the Fe_5C_2 surface. (b) Fe 2p XPS spectrum, which indicates the existence of an Fe_3O_4 phase on the Fe_5C_2 surface. (c) C 1s XPS spectrum and (d) Raman spectrum, which suggest the coexistence of amorphous and graphitic carbon on the surface of Fe_5C_2 NPs.

(Figure 3d), the G peak at 1600 cm^{-1} and the D peak at 1328 cm^{-1} indicate the presence of graphitic carbon.[38,39] This is consistent with previous reports claiming the coexistence of amorphous carbon and graphitic carbon on the iron carbide surface.[40−42] As carbon was the most abundant element in the surface, it can be reasonably concluded that the as-synthesized Fe_5C_2 NPs had a small amount of Fe_3O_4 phase and an outer amorphous graphitic carbon decoration except for dominant Fe_5C_2 components. It is worth noting that no peak for bromide (a catalyst poison for FTS) was observed in the XPS study, which suggests that bromide did not exist on the surface of the Fe_5C_2 NPs (Figure S3).

3.2. Synthetic Mechanism. In a typical synthetic procedure, the introduction of bromide was found to be the key factor in the formation of Fe_5C_2 NPs. With the presence of bromide, well-crystallized Fe_5C_2 NPs were prepared (Figure 4a), while an amorphous product was obtained when bromide was absent from the system (Figure 4b). The difference in the chemical natures of the two samples could also be discriminated by the Fe 2p XPS spectra (Figure 4c,d). Though in both samples the presence of two peaks at ∼724.5 and ∼710.8 eV indicated the existence Fe_3O_4,[43] the other two peaks at 707.0 and 719.9 eV in Figure 4c are associated with Fe_5C_2, suggesting that the external surface of the iron carbide NPs was only slightly oxidized compared with NPs prepared using the bromide-free approach. This is consistent with an early report suggesting that halogen could enhance the crystallinity of Fe NPs by decreasing the decomposition rate of $Fe(CO)_5$ and consequently improving the antioxidation property of the as-synthesized Fe NPs.[44]

To determine the Fe source for the Fe_5C_2 NPs, we studied the phase conversion of the resultant NPs in reactions involving bromide at 598 and 623 K. Well-crystallized Fe NPs were obtained at 598 K (Figure 5a). As the reaction system was further heated to 623 K, these Fe NPs were carbonized to Fe_5C_2 NPs (Figure 5b). Therefore, the Fe NPs are considered to be the iron source for Fe_5C_2.

dx.doi.org/10.1021/ja305048p | J. Am. Chem. Soc. 2012, 134, 15814−15821

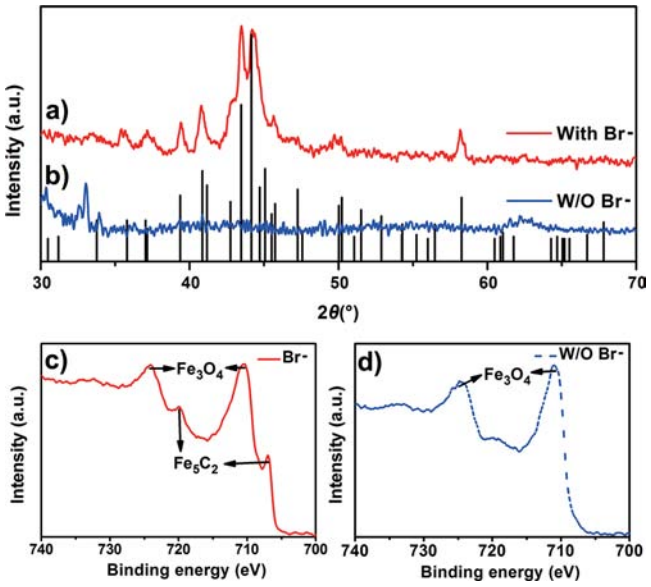

Figure 4. (a, b) XRD patterns and (c, d) Fe 2p XPS spectra of NPs synthesized using (a, c) the reaction involving bromide (JCPDS no. 36-1248) and (b, d) the bromide-free reaction.

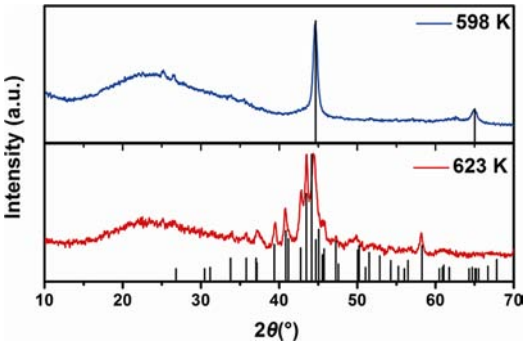

Figure 5. XRD patterns of NPs generated from reactions at (a) 598 K (JCPDS no. 06-0696) and (b) 623 K (JCPDS no. 36-1248).

On the other hand, to identify the carbon source, three reactions were designed, as shown in Table 1. Reaction A was the conventional reaction involving bromide. Reaction B was similar to reaction A except for the absence of $Fe(CO)_5$. Reaction C was similar to reaction A except for the absence of bromide. During each reaction process, we separately extracted solutions from the reaction mixture when the temperature reached 453, 543 and 623 K; these are designated as A/B/C-453K, A/B/C-543K, and A/B/C-623K, respectively. The nine samples were then studied by GC−MS and FTIR.

Table 1. Reactants for Reactions A, B, and C

reaction	solvent	precursor	inducing agent	remarks
A	octadecylamine	$Fe(CO)_5$	CTAB	conventional reaction
B	octadecylamine	none	CTAB	conventional reaction without $Fe(CO)_5$
C	octadecylamine	$Fe(CO)_5$	none	conventional reaction without CTAB

For the reactions at 453 K, the contents of all of the solutions were 1-hexadecanamine [impurity, retention time (t_R) ≈15.4] and 1-octadecanamine (t_R ≈ 17.4) (Figure S4). However, when the temperature reached 543 K, peaks due to 1-hexadecanenitrile (t_R ≈ 15.8) and 1-octadecanenitrile (t_R ≈ 17.8) appeared in A-543K and C-543K, indicating the transformation of $-NH_2$ to $-CN$ in both reactions (Figure 6a). When the reaction temperature was further increased to 623 K, it was observed that all of the amines were converted to nitriles in both A-623K and C-623K (Figure 6b) while no such conversion was observed in B-623K, which demonstrates that Fe can catalyze the dehydrogenation of $-NH_2$ at 543 K or above. Moreover, in addition to 1-hexadecanenitrile and 1-octadecanenitrile, A-623K also contained plenty of unsaturated hydrocarbons and shorter-chain nitriles, which were barely observed in C-623K. This shows that the nitriles in reaction A underwent a C−C bond cleavage process at ~623 K, while those in reaction C did not. FTIR characterization further confirmed the GC−MS results mentioned above. In the FTIR spectra of A-623K, C-623K, and the original solvent, the vanishing of the absorbance due to the $C-NH_2$ bond (doublet at ~3475 and ~3336 cm^{-1}) with the simultaneous growth of the C≡N band (~2245 cm^{-1}) and the C═C band (doublet at ~1668 and ~1639 cm^{-1}) implies the conversion of amines to alkenes and cyanides (Figure S5). Moreover, the A-623K spectrum shows much stronger bands for both C≡N and C═C compared with the C-623K spectrum. This indicates that the A-623K sample contains much greater amounts of cyanides and alkenes than C-623K, which is consistent with the GC−MS results. Therefore, it can be concluded that the unsaturated hydrocarbons act as the carbon source for the Fe_5C_2 NPs (Figure S6).

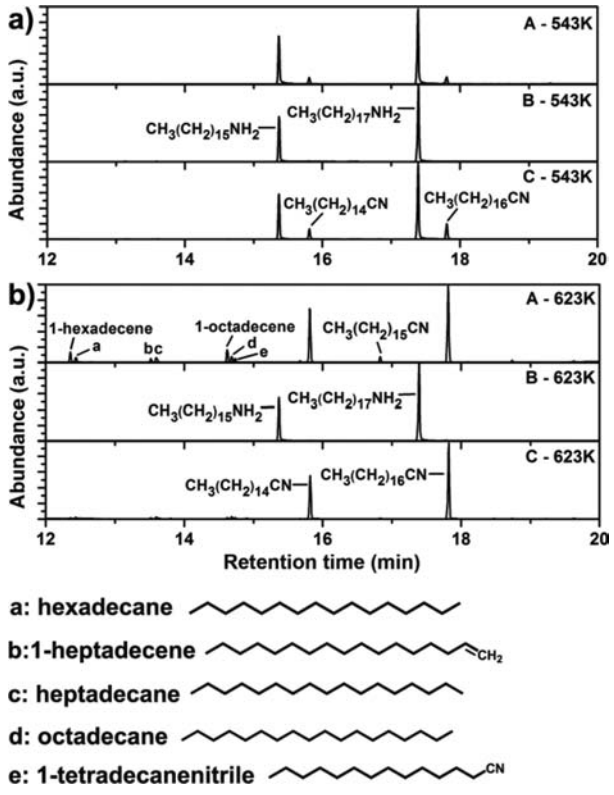

Figure 6. GC−MS chromatograms obtained from the reaction solutions extracted at (a) 543 and (b) 623 K.

Therefore, we can propose the mechanism for the synthesis of the Fe_5C_2 NPs illustrated in Scheme 1. With the participation of bromide, the well-crystallized Fe NPs are first formed by the decomposition of $Fe(CO)_5$ at ~453 K, and these

dx.doi.org/10.1021/ja305048p | J. Am. Chem. Soc. 2012, 134, 15814−15821

Scheme 1. Schematic Illustration of the Formation Mechanism of Fe_5C_2 NPs

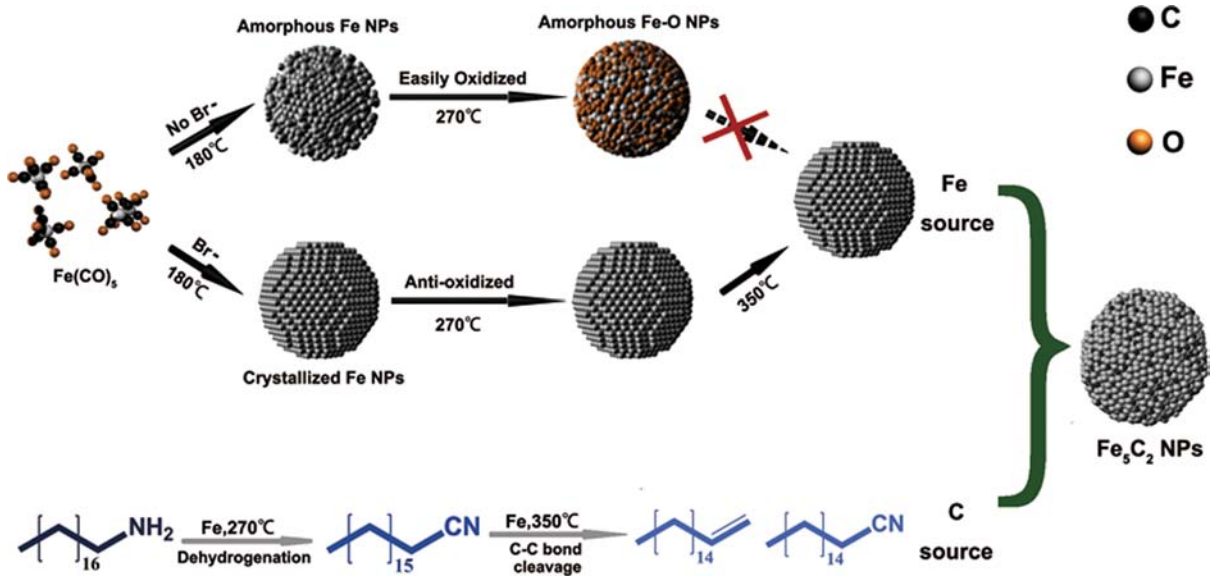

Fe NPs serve as the Fe source for the Fe_5C_2 NPs. Meanwhile, the as-synthesized Fe NPs catalyze the dehydrogenation of the amine group at ~543 K. Next, with an increase in temperature to 623 K, the Fe NPs can also catalyze the pyrolysis of the long-chain cyanides (note that Fe was previously proved to be capable of catalyzing the cleavage of C−C bonds of organonitriles[45−49]). The resulting unsaturated hydrocarbons and cyanides serve as carbon source and further carbonize the Fe NPs to Fe_5C_2 at 623 K. However, in the reaction where bromide is absent, amorphous Fe NPs are formed. As reported previously, amorphous Fe NPs are easily oxidized.[50] Therefore, at a high temperature of ~573 K, the amorphous Fe NPs are likely oxidized by residual oxygen or oxygenous groups even under an inert atmosphere and thus lose their ability to catalyze the C−C bond cleavage of the organonitriles.

To verify this mechanism from another perspective, we added the strong reducing agent *n*-butyllithium into a bromide-free reaction. After the mixture was degassed for 1 h, 1 mmol of *n*-butyllithium was injected at 328 K under an inert atmosphere. The following process was the same as in the synthesis of 20 nm Fe_5C_2 NPs. XRD and XPS characterizations were performed on the as-synthesized NPs, and the results are shown in Figure 7 b,e; XRD patterns and XPS spectra of NPs generated from reactions with bromide (Figure 7 a,d) and without bromide (Figure 7 c,f) are also shown for comparison. The XRD pattern in Figure 7b indicates that Fe_5C_2 was synthesized in the reaction. However, the broad reflections at 42−45° reveal the less crystalline nature of the Fe_5C_2 phase. The reflections at 33 and 62° also indicate the existence of Fe_3O_4 as the oxidation product. The peaks at 707.0 and 719.9 eV in the Fe 2p XPS spectrum (Figure 7e) also demonstrate the existence of Fe_5C_2. Hence, this experiment further validates that the bromide induces and improves the crystallinity of the Fe NPs. Subsequently, the crystalline Fe particles facilitate the formation of Fe_5C_2 NPs. Therefore, the bromide is the key inducing agent in the synthesis of Fe_5C_2 NPs under these mild conditions.

3.3. Catalytic Properties. TPSR experiments were used to characterize the catalytic activity of Fe_5C_2 NPs in order to investigate the reaction process on the catalyst surface under

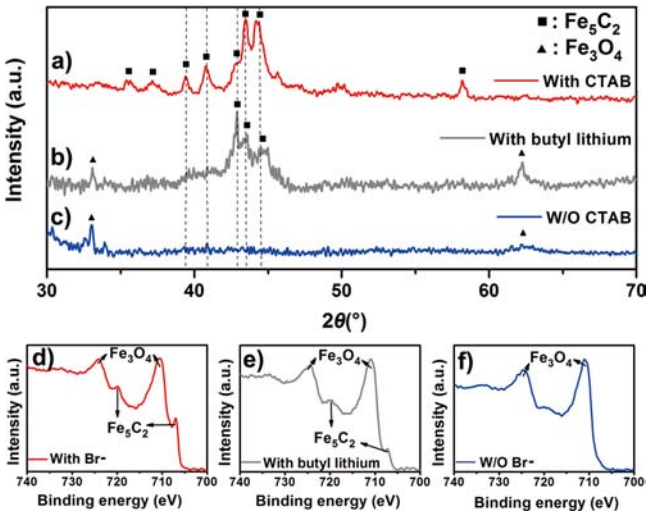

Figure 7. XRD patterns and Fe 2p XPS spectra for products generated from reactions with (a, d) bromide, (b, e) *n*-butyllithium, and (c, f) neither of them.

reaction conditions. In the experiment, TPSRs were carried out in two individual FTS processes, one using supported Fe_5C_2 NPs and the other hematite NPs as catalysts. It should be noted that neither catalyst underwent any pretreatment. In both reactions, the temperature was raised from 303 to 543 K at 3 K/min and then kept at 543 K. The time was counted as soon as the temperature reached 543 K, as shown in Figure 8. In the Fe_5C_2-catalyzed FTS, the reaction started immediately when the temperature reached 543 K, as indicated by the consumption of syngas (CO and H_2) and simultaneous generation of hydrocarbons (Figure 8a). In the case of the Fe_2O_3-catalyzed FTS, however, the reaction did not start even when the temperature was kept at 543 K for over 3400 s (Figure 8b). Instead, only after reduction at 653 K for 16 h and then treatment in the syngas stream at 543 K, where Fe_2O_3 was first transformed into metallic Fe and then iron carbide, could the formation of hydrocarbon be observed (Figure S7). Therefore, the results clearly indicate that the induction period

dx.doi.org/10.1021/ja305048p | J. Am. Chem. Soc. 2012, 134, 15814−15821

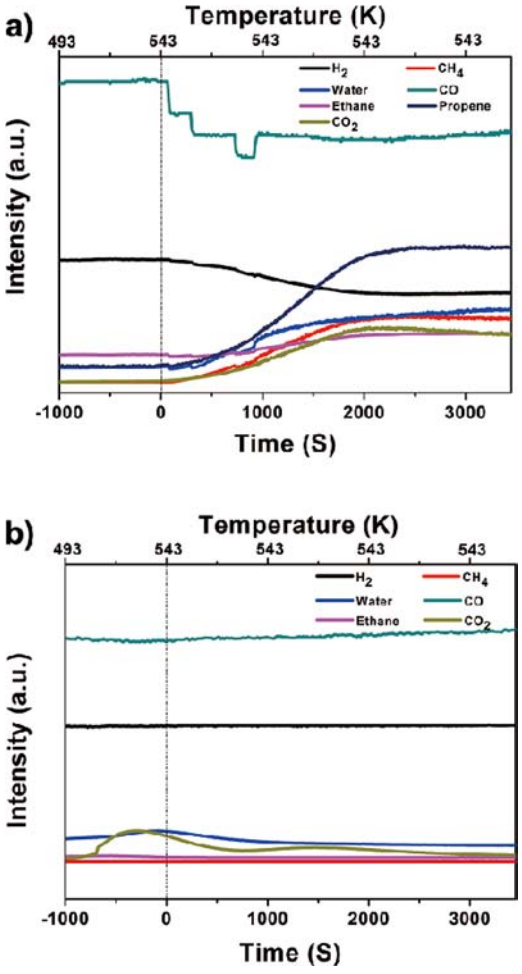

Figure 8. Time and temperature dependent TPSR diagrams for a) Fe_5C_2 NPs/SiO_2 and b) Fe_2O_3/SiO_2 catalysts. Note that the time was counted 0 as soon as the temperature reached 543K as indicated by the dot-line.

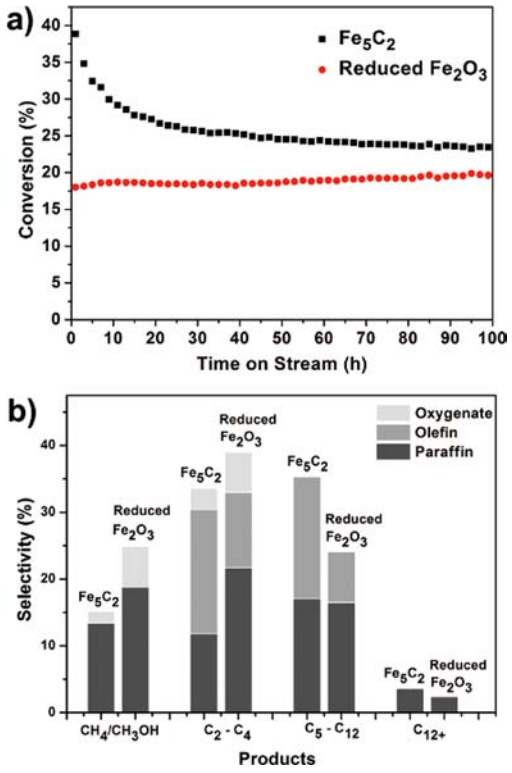

Figure 9. Overall catalytic performance of Fe_5C_2 NPs/SiO_2 and reduced Fe_2O_3/SiO_2 catalysts: (a) CO conversion and (b) product selectivity.

for FTS can be eliminated by using the Fe_5C_2 catalyst (i.e., that Fe_5C_2 is an active phase for FTS).

The CO conversion and product selectivity of the Fe_5C_2 NPs as the catalyst in the FTS reaction were investigated. A typical iron catalyst for FTS, H_2-reduced hematite catalyst, was used as a control to provide a better illustration of the catalytic performance of the Fe_5C_2 NPs. It is worth noting that no promoters or additives were added, since the purpose was to investigate the intrinsic catalytic performance of the Fe_5C_2 NPs. The overall FTS catalytic performances of the two catalysts are shown in Figure 9. The initial CO conversion rate with the Fe_5C_2 NPs was 39% and decreased to 24% after FTS for 100 h. For the reduced hematite catalyst, however, the CO conversion slightly increased from 18 to 20% after FTS for 100 h. This suggests that Fe_5C_2 NPs have higher catalytic activity for FTS in comparison with the conventional H_2-reduced hematite catalyst. With respect to the selectivity, the Fe_5C_2 NP-catalyzed FTS exhibited a good C_{5+} hydrocarbon selectivity of ~39%. Additionally, in the C_2-C_4 composition range (gaseous products), the more useful olefins represented 61% of the whole C_2-C_4 products and 19% of all carbon products, which suggests that the Fe_5C_2 NPs are also a desirable catalyst for light olefins in the gaseous range. For comparison, the H_2-reduced hematite showed a C_{5+} selectivity of 26% and light olefin selectivity of 11%. Additionally, the chain-growth probability (α) of the Fe_5C_2 NPs was 0.68, while the reduced hematite catalyst presented dual α-value character (Figure S8).[51] Generally, the Fe_5C_2 NPs exhibited better catalytic performance in terms of activity and longer-chain hydrocarbon selectivity compared with conventional reduced hematite.

As shown in Figure 9a, the CO conversion for FTS catalyzed by Fe_5C_2 NPs underwent a rapid drop within the initial 30 h of reaction. To provide a better understanding of the underlying mechanism, Fe_5C_2 NPs after 30 h of FTS were examined using XRD and TEM. As shown in Figure 10 a,b, the Fe_5C_2 NPs after 30 h reaction showed neither a change in morphology nor particle aggregation. However, those Fe_5C_2 NPs were encapsulated in residual hydrocarbons and slightly oxidized. XPS was applied to characterize further the surface properties of the Fe_5C_2 NPs. Unexpectedly, there was no Fe signal from the Fe_5C_2 NPs after 30 h of reaction (Figure 11), further proving that the Fe_5C_2 NPs were fully encapsulated by hydrocarbons. Similarly, no Fe signal was recorded from the used hematite-based catalyst either, which suggests that the hydrocarbon shielding is not the root cause of the activity drop of the Fe_5C_2 NP catalyst. Instead, the partial oxidation of the Fe_5C_2 due to the reaction between the carbide and the H_2O and CO_2 formed in the FTS is responsible for the catalyst deactivation.

4. CONCLUSION

A facile one-pot wet-chemistry strategy for the synthesis of Fe_5C_2 NPs was developed. Investigation of the synthetic mechanism of Fe_5C_2 NPs showed that bromide enhanced the antioxidized nature of the Fe NPs and that such Fe NPs are crucial for the subsequent formation of Fe_5C_2. Furthermore, the

dx.doi.org/10.1021/ja305048p | J. Am. Chem. Soc. 2012, 134, 15814−15821

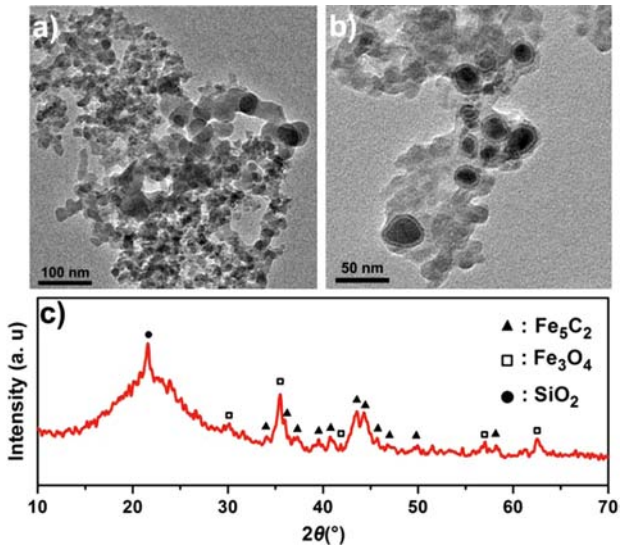

Figure 10. (a, b) TEM images and (c) XRD pattern for the Fe_5C_2 NPs after 30 h of FTS reaction.

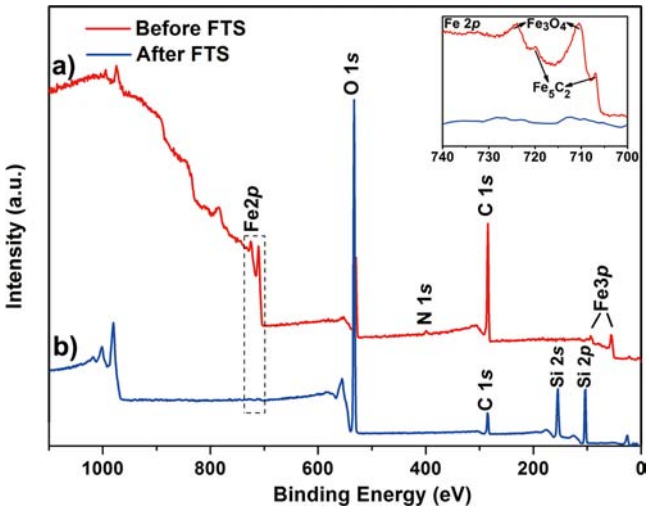

Figure 11. XPS spectra for Fe_5C_2 NPs (a) before and (b) after 30 h of FTS reaction. The inset is an amplification of the portion of the spectrum indicated by the dashed line.

as-synthesized Fe_5C_2 NPs were investigated as catalysts in the FTS reaction. Compared with a conventional reduced hematite catalyst, the Fe_5C_2 NPs exhibited intrinsic catalytic activity as well as enhanced catalytic performance, which shows that Fe_5C_2 is an active phase for FTS. Generally, this study not only provides a facile method for the synthesis of iron carbide NPs but also proposes a new approach for obtaining a better understanding of the FTS mechanism. In addition, this work may also become a milestone achievement in producing large-scale novel FTS catalysts for new energy conversion.

■ ASSOCIATED CONTENT

Supporting Information

XRD patterns of Fe_5C_2 NPs prepared using various bromides as inducing agents, XRD patterns and TEM images for 10 nm Fe_5C_2 NPs, XRD and XPS studies of NPs generated from bromide-free reaction, GC–MS profile and FTIR spectra of the extracted solutions, TPSR for the reduced Fe_2O_3 catalyst, and propagation factors for the Fe_5C_2 and reduced Fe_2O_3 catalysts. This material is available free of charge via the Internet at http://pubs.acs.org.

■ AUTHOR INFORMATION

Corresponding Author

hou@pku.edu.cn; dma@pku.edu.cn

Notes

The authors declare no competing financial interest.

■ ACKNOWLEDGMENTS

This work was supported in part by the NSFC (51125001, 51172005, 90922033, and 20773121), the National Basic Research Program of China (2010CB934601 and 2011CB201402), a New Century Excellent Talents in University Award from the Education Ministry of China (NCET-09-0177), and the Yok Ying Tung Foundation (122043). We thank the SSRF for providing the beamline.

■ REFERENCES

(1) Cao, D. B.; Zhang, F. Q.; Li, Y. W.; Wang, J. G.; Jiao, H. J. *J. Phys. Chem. B* **2005**, *109*, 10922.
(2) Greenwood, N. N.; Earnshaw, A. *Chemistry of the Elements*; Pergamon: Oxford, U.K., 1984; p 318.
(3) Faraoun, H. I.; Zhang, Y. D.; Esling, C.; Aourag, H. *J. Appl. Phys.* **2006**, *99*, No. 093508.
(4) Cao, D. B.; Zhang, F. Q.; Li, Y. W.; Jiao, H. J. *J. Phys. Chem. B* **2004**, *108*, 9094.
(5) Biswas, A. K. *Indian J. Hist. Sci.* **1994**, *29*, 579.
(6) Schnepp, Z.; Wimbush, S. C.; Antonietti, M.; Giordano, C. *Chem. Mater.* **2010**, *22*, 5340.
(7) Giordano, C.; Kraupner, A.; Wimbush, S. C.; Antonietti, M. *Small* **2010**, *6*, 1859.
(8) Kraupner, A.; Antonietti, M.; Palkovits, R.; Schlicht, K.; Giordano, C. *J. Mater. Chem.* **2010**, *20*, 6019.
(9) Deck, C. P.; Vecchio, K. *Carbon* **2006**, *44*, 267.
(10) Yu, G. B.; Sun, B.; Pei, Y.; Xie, S. H.; Yan, S. R.; Qiao, M. H.; Fan, K. N.; Zhang, X. X.; Zong, B. N. *J. Am. Chem. Soc.* **2010**, *132*, 935.
(11) de Smit, E.; Cinquini, F.; Beale, A. M.; Safonova, O. V.; van Beek, W.; Sautet, P.; Weckhuysen, B. M. *J. Am. Chem. Soc.* **2010**, *132*, 14928.
(12) Janbroers, S.; Louwen, J. N.; Zandbergen, H. W.; Kooyman, P. J. *J. Catal.* **2009**, *268*, 235.
(13) Bukur, D. B.; Okabe, K.; Rosynek, M. P.; Li, C. P.; Wang, D. J.; Rao, K. R. P. M.; Huffman, G. P. *J. Catal.* **1995**, *155*, 353.
(14) de Smit, E.; Weckhuysen, B. M. *Chem. Soc. Rev.* **2008**, *37*, 2758.
(15) Wen, Z.; Ci, S.; Zhang, F.; Feng, X.; Cui, S.; Mao, S.; Luo, S.; He, Z.; Chen, J. *Adv. Mater.* **2012**, *24*, 1399.
(16) Browning, L. C.; Dewitt, T. W.; Emmett, P. H. *J. Am. Chem. Soc.* **1950**, *72*, 4211.
(17) Browning, L. C.; Emmett, P. H. *J. Am. Chem. Soc.* **1951**, *73*, 581.
(18) Kummer, J. T.; Dewitt, T. W.; Emmett, P. H. *J. Am. Chem. Soc.* **1948**, *70*, 3632.
(19) Podgurski, H. H.; Kummer, J. T.; Dewitt, T. W.; Emmett, P. H. *J. Am. Chem. Soc.* **1950**, *72*, 5382.
(20) Hager, G. T.; Bi, X. X.; Derbyshire, F. J.; Eklund, P. C.; Stencel, J. M. *Abstr. Pap.—Am. Chem. Soc.* **1991**, *202*, 51.
(21) Sethuraman, A. R.; Stencel, J. M.; Rubel, A. M.; Cavin, B.; Hubbard, C. R. *J Vac. Sci. Technol., A* **1994**, *12*, 443.
(22) Stencel, J. M.; Eklund, P. C.; Bi, X. X.; Davis, B. H.; Hager, G. T.; Derbyshire, F. J. *Stud. Surf. Sci. Catal.* **1993**, *75*, 1797.
(23) Yang, K. Y.; Xu, W.; Zhang, Y.; Zheng, W. T.; Wang, X. *Chem. Res. Chin. Univ.* **2010**, *26*, 348.
(24) Song, H. H.; Chen, X. H. *Chem. Phys. Lett.* **2003**, *374*, 400.
(25) Schnepp, Z.; Yang, W.; Antonietti, M.; Giordano, C. *Angew. Chem., Int. Ed.* **2010**, *49*, 6564.
(26) Giordano, C.; Erpen, C.; Yao, W. T.; Milke, B.; Antonietti, M. *Chem. Mater.* **2009**, *21*, 5136.

(27) Dong, X. L.; Zhang, Z. D.; Xiao, Q. F.; Zhao, X. G.; Chuang, Y. C.; Jin, S. R.; Sun, W. M.; Li, Z. J.; Zheng, Z. X.; Yang, H. *J. Mater. Sci.* **1998**, *33*, 1915.
(28) Caceres, P. G. *Mater. Charact.* **2006**, *56*, 26.
(29) Su, J.; Gao, Y. H.; Che, R. C. *Mater. Lett.* **2010**, *64*, 680.
(30) Koniger, A.; Hammerl, C.; Zeitler, M.; Rauschenbach, B. *Phys. Rev. B* **1997**, *55*, 8143.
(31) Giordano, C.; Erpen, C.; Yao, W. T.; Antonietti, M. *Nano Lett.* **2008**, *8*, 4659.
(32) Giordano, C.; Antonietti, M. *Nano Today* **2011**, *6*, 366.
(33) Leckel, D. *Energy Fuels* **2009**, *23*, 2342.
(34) Huo, C. F.; Li, Y. W.; Wang, J. G.; Jiao, H. J. *J. Am. Chem. Soc.* **2009**, *131*, 14713.
(35) Lohitharn, N.; Goodwin, J. G.; Lotero, E. *J. Catal.* **2008**, *255*, 104.
(36) Park, J. Y.; Lee, Y. J.; Khanna, P. K.; Jun, K. W.; Bae, J. W.; Kim, Y. H. *J. Mol. Catal. A: Chem.* **2010**, *323*, 84.
(37) Jia, C. J.; Sun, L. D.; Luo, F.; Han, X. D.; Heyderman, L. J.; Yan, Z. G.; Yan, C. H.; Zheng, K.; Zhang, Z.; Takano, M.; Hayashi, N.; Eltschka, M.; Klaui, M.; Rudiger, U.; Kasama, T.; Cervera-Gontard, L.; Dunin-Borkowski, R. E.; Tzvetkov, G.; Raabe, J. *J. Am. Chem. Soc.* **2008**, *130*, 16968.
(38) Ferrari, A. C.; Meyer, J. C.; Scardaci, V.; Casiraghi, C.; Lazzeri, M.; Mauri, F.; Piscanec, S.; Jiang, D.; Novoselov, K. S.; Roth, S.; Geim, A. K. *Phys. Rev. Lett.* **2006**, *97*, No. 187401.
(39) Fjellvåg, H.; Karen, P. *Inorg. Chem.* **1992**, *31*, 3260.
(40) Jackson, N. B.; Datye, A. K.; Mansker, L.; O'Brien, R. J.; Davis, B. H. *Stud. Surf. Sci. Catal.* **1997**, *111*, 501.
(41) Datye, A. K.; Jin, Y. M.; Xu, H. F. *Microsc. Microanal.* **2006**, *12*, 124.
(42) Xu, J.; Bartholomew, C. R. *J. Phys. Chem. B* **2005**, *109*, 2392.
(43) Fujii, T.; de Groot, F. M. F.; Sawatzky, G. A.; Voogt, F. C.; Hibma, T.; Okada, K. *Phys. Rev. B.* **1999**, *59*, 3195.
(44) Sun, S. H.; Lacroix, L.-M.; Frey Huls, N.; Ho, D.; Sun, X. L.; Cheng, K.; Sun, S. H. *Nano Lett.* **2011**, *11*, 1641.
(45) Jones, W. D.; Evans, M. E. *Organometallics* **2011**, *30*, 3371.
(46) Jana, U.; Biswas, S.; Maiti, S. *Eur. J. Org. Chem.* **2010**, 2861.
(47) Cheng, L.; Zhao, Y. Y.; Bi, X. X.; Bi, S. W. *THEOCHEM* **2008**, *869*, 59.
(48) Chatani, N.; Tobisu, M. *Chem. Soc. Rev.* **2008**, *37*, 300.
(49) Huber, D. L. *Small* **2005**, *1*, 482.
(50) Sun, S. H.; Peng, S.; Wang, C.; Xie, J. *J. Am. Chem. Soc.* **2006**, *128*, 10676.
(51) Huff, G. A., Jr.; Satterfield, C. N. *J. Catal.* **1984**, *85*, 370.